

Indigo: A Natural Molecular Passivator for Efficient Perovskite Solar Cells

Junjun Guo, Jianguo Sun, Long Hu, Shiwen Fang, Xufeng Ling, Xuliang Zhang, Yao Wang, Hehe Huang, Chenxu Han, Claudio Cazorla, Yingguo Yang, Dewei Chu, Tom Wu, Jianyu Yuan,* and Wanli Ma*

Organic–inorganic hybrid lead halide perovskite solar cells have made unprecedented progress in improving photovoltaic efficiency during the past decade, while still facing critical stability challenges. Herein, the natural organic dye Indigo is explored for the first time to be an efficient molecular passivator that assists in the preparation of high-quality hybrid perovskite film with reduced defects and enhanced stability. The Indigo molecule with both carbonyl and amino groups can provide bifunctional chemical passivation for defects. In-depth theoretical and experimental studies show that the Indigo molecules firmly binds to the perovskite surfaces, enhancing the crystallization of perovskite films with improved morphology. Consequently, the Indigo-passivated perovskite film exhibits increased grain size with better uniformity, reduced grain boundaries, lowered defect density, and retarded ion migration, boosting the device efficiency up to 23.22%, and $\approx 21\%$ for large-area device (1 cm^2). Furthermore, the Indigo passivation can enhance device stability in terms of both humidity and thermal stress. These results provide not only new insights into the multipassivation role of natural organic dyes but also a simple and low-cost strategy to prepare high-quality hybrid perovskite films for optoelectronic applications based on Indigo derivatives.

1. Introduction

The organic–inorganic lead halide perovskites have emerged and quickly become the most promising materials for solution-processed solar cells.^[1,2] These hybrid semiconductors exhibit unique properties such as high carrier mobility, long carrier diffusion length, high defect tolerance, and low exciton


binding energy.^[3–6] Benefiting from these unique properties, the power conversion efficiency (PCE) of perovskite solar cells (PSCs) has rapidly increased from initial $\approx 3\%$ to now 25.5%,^[7–9] situating it at the forefront of the third-generation solar cells.^[10,11] Unfortunately, these ionic hybrid perovskite materials are extremely sensitive to light,^[12,13] heat,^[14] and moisture,^[15] resulting in unstable crystal structures. During the past decade, numerous passivating methods have been developed to enhance both efficiency and long-term stability of hybrid PSCs.^[16–18]

In these polycrystalline perovskite films, defects formed at either surface or grain boundaries have been widely reported to significantly restrict carriers transport and crystal stability, which further deteriorates the device performance.^[19,20] Indeed, a large number of defects are generated during the film crystallization process due to the low formation energy and soft lattice character of the perovskite crystals.^[21,22]

Besides, the ionic nature of hybrid halide perovskite leads to unfavorable carrier recombination and ion migration in the perovskite films, resulting in unsatisfactory efficiency or stability of the devices.^[23,24] In particular, the crystallization process is accompanied by the ubiquitous formation of imperfections at grain boundaries and surfaces, metallic lead clusters, and intrinsic point defects.^[24–26] Among them, intrinsic site

J. Guo, J. Sun, S. Fang, X. Ling, X. Zhang, Y. Wang, H. Huang, C. Han, J. Yuan, W. Ma
Institute of Functional Nano and Soft Materials (FUNSOM)
Jiangsu Key Laboratory for Carbon-Based Functional Materials and Devices
Soochow University
199 Ren-Ai Road, Suzhou Industrial Park, Suzhou, Jiangsu 215123, P. R. China
E-mail: jyyuan@suda.edu.cn; wlma@suda.edu.cn
L. Hu
School of Engineering
Macquarie University
Sydney, New South Wales 2109, Australia

C. Cazorla
Department de Física
Universitat Politècnica de Catalunya
Campus Nord B4-B5, Barcelona E-08034, Spain
Y. Yang
Shanghai Synchrotron Radiation Facility
Shanghai Institute of Applied Physics
Chinese Academy of Sciences
Shanghai 201204, P. R. China
D. Chu, T. Wu
School of Materials Science and Engineering
University of New South Wales (UNSW)
Sydney, NSW 2052, Australia

 The ORCID identification number(s) for the author(s) of this article can be found under <https://doi.org/10.1002/aenm.202200537>.

DOI: 10.1002/aenm.202200537

defects include uncoordinated $\text{Pb}^{2+}/\text{I}^-$, Pb-I antisites/impurities and surface defects due to terminally growth of perovskite crystals, which significantly deteriorates the optoelectronic properties of the PSCs.^[27,28] In order to eliminate these unwanted defects, engineering strategies involving component,^[29,30] dimensionality,^[31,32] grain boundary,^[25] additive,^[33] and antisolvent/solution^[34] have been intensively explored. Among these strategies, antisolvent treatments using functional passivating agents such as organic molecules,^[23] polymers,^[35] and inorganic nanocrystals^[36] have been reported to effectively optimize the crystallization process as well as passivate the defects at surfaces and grain boundaries. In general, most effective passivator molecules contain isolated electron pairs isolated electron pairs in molecules framework (Lewis base groups^[38]), such as carbonyl (C=O),^[26] sulfoxide (S=O),^[37] phosphate (P=O),^[20] and cyano (–CN).^[39] Therefore, the passivating mechanism is interaction between passivating agent (Lewis bases) with positively charged intrinsic site defects on the surface of perovskite (Lewis acids).^[28] Yang et al. demonstrated that the amino group (–NH) in theophylline can interact with the I^- in the PbI_6^{2-} octahedron via hydrogen bonding and assist the carbonyl group (C=O) to interact with the uncoordinated Pb^{2+} .^[18] Quite recently, Gao et al. reported that passivation of Pb-I antisites by –NH group and the metal Pb clusters by –OH protonic group using the tailored molecule naphthalene-1,8-dicarboximide.^[38]

Inspired by our previous study in Isoindigo-based conjugated materials,^[40] here, we report a natural small organic dye, Indigo, as a new molecular passivator for efficient PSCs. The Indigo molecule bears desired carbonyl and amino functional groups, showing stability under heat and moisture stresses. In addition, it is very low-cost with abundant availability in nature, which makes Indigo ideal material for developing high-performance PSCs. The carbonyl group (electron pair donor) in the Lewis base Indigo molecule can interact with the unfilled p-orbitals Lewis acid Pb^{2+} , Pb-I antisites defects on the perovskite surface, and the amino group can interact with the I^- sites. In addition, the hydrogen bonding between Indigo molecules and perovskite surfaces could restrain ion migration,^[16] thus enhancing the stability of perovskite crystal structure. Resultantly, the PCE of the Indigo passivated PSCs is enhanced from 20.18% to 23.22% with simultaneously increased short-circuit current density (J_{sc}), open-circuit voltage (V_{oc}), and fill factor (FF) as well as reduced hysteresis relative to the control one. Furthermore, owing to the hydrogen bonding upon Indigo passivation and increased perovskite surface hydrophobicity, the stability of the PSCs under humidity and thermal stress are both significantly enhanced.

2. Results and Discussion

As shown in Figure 1a, the 3D perovskite film with a composition of $\text{Cs}_{0.05}\text{FA}_{0.85}\text{MA}_{0.10}\text{Pb}(\text{I}_{0.90}\text{Br}_{0.10})_3$ was chosen and prepared according to the reported method.^[31] The mixed perovskite film was deposited using a one-step method containing antisolvent treatment. During the antisolvent process, Indigo was dissolved in chlorobenzene (CB) at the optimal concentration to post-treat the 3D perovskite film via a dripping approach

(see the Experimental Section for details), followed by annealing at 100 °C for 60 min. The concentrations of Indigo were optimized to be 0.05 mg mL⁻¹ according to the statistical analysis of PCE (Table S1 and Figure S1, Supporting Information). To gain a fundamental understanding of the interactions between Indigo molecules and 3D mixed perovskite, the Fourier transform infrared (FTIR) spectroscopy and X-ray photoelectron spectroscopy (XPS) were performed. As illustrated in Figure 1b (with the full regions shown in Figure S2, Supporting Information), the characteristic peaks at around 1460 cm⁻¹ are attributed to the conjugated aromatic ring.^[16,26] More interestingly, the characteristic stretching vibration of the C=O in Indigo slightly shifts from 1630 to ≈1614 cm⁻¹ and the stretching vibration intensity of –NH decreases upon deposition onto the perovskite film, suggesting the chemical interaction between the Indigo molecule and the perovskite.^[16,19] More direct evidence about the interaction between Indigo molecule and perovskite surface is provided by the XPS characterization (Figure 1c,d). In comparison with the pristine perovskite film, the Indigo-treated film exhibits shift to lower binding energy positions, suggesting the formation of chemical bonding between Indigo molecule and perovskite.^[31,35] In specific, the characteristic peaks of Pb in the pristine thin film shows two peaks located at 142.21 and 137.26 eV, corresponding to the Pb 4f_{5/2} and Pb 4f_{7/2} core level, respectively (Figure 1c), and both peaks undergo ≈0.40 eV shift to the lower binding energy positions. Meanwhile, in the core level spectra of I, we observe the similar downshift after the Indigo treatment (Figure 1d). According to the previous reports, such a shift may be attributed to the coordination bonding between O and Pb via Lewis based-acid interaction between the C=O bond of Indigo and the Pb^{2+} in the thin film as well as the interaction between –NH and perovskite surface (halide I^-) via hydrogen bonding.^[38,41] Based on these results, a schematic diagram of defect passivation mechanism for the Indigo post-treatment is shown in Figure 1e.

To gain insight into the passivation mechanism and interaction between Indigo and perovskite surface, first-principles calculations based on density functional theory (DFT)^[42] were carried out. The generalized gradient approximation^[43] in the Perdew–Burke–Ernzerhof flavor is used to describe the effects of electronic exchange and correlation. The projector-augmented wave method^[44] is employed to represent the ionic cores. A 12-atom unit cell of FAPbI_3 (in order to simplify the calculations) is first relaxed with a Monkhorst–Pack k -point mesh of $8 \times 8 \times 8$. Subsequently, a $3 \times 3 \times 2$ slab FAPbI_3 system reproducing the surface Miller index <001> is generated by adding a vacuum region of 20 Å thickness, in which the Pb and I ions are exposed. Detailed calculation parameters can be found in the Supporting Information. The DFT calculations show that the oxygen atoms in the Indigo molecule tend to form bonds with the surface Pb^{2+} ions of FAPbI_3 , as demonstrated by binding energy, charge density difference (CDD, shown in Figure 2a), and Bader charge analysis. In particular, based on the formula

$$E_{\text{binding}} = E_{\text{indigo@FAPbI}_3} - E_{\text{indigo}} - E_{\text{FAPbI}_3\text{slab}} \quad (1)$$

A large Indigo binding energy of –1.52 eV is estimated for a non-defective FAPbI_3 surface, which suggests chemical adsorption

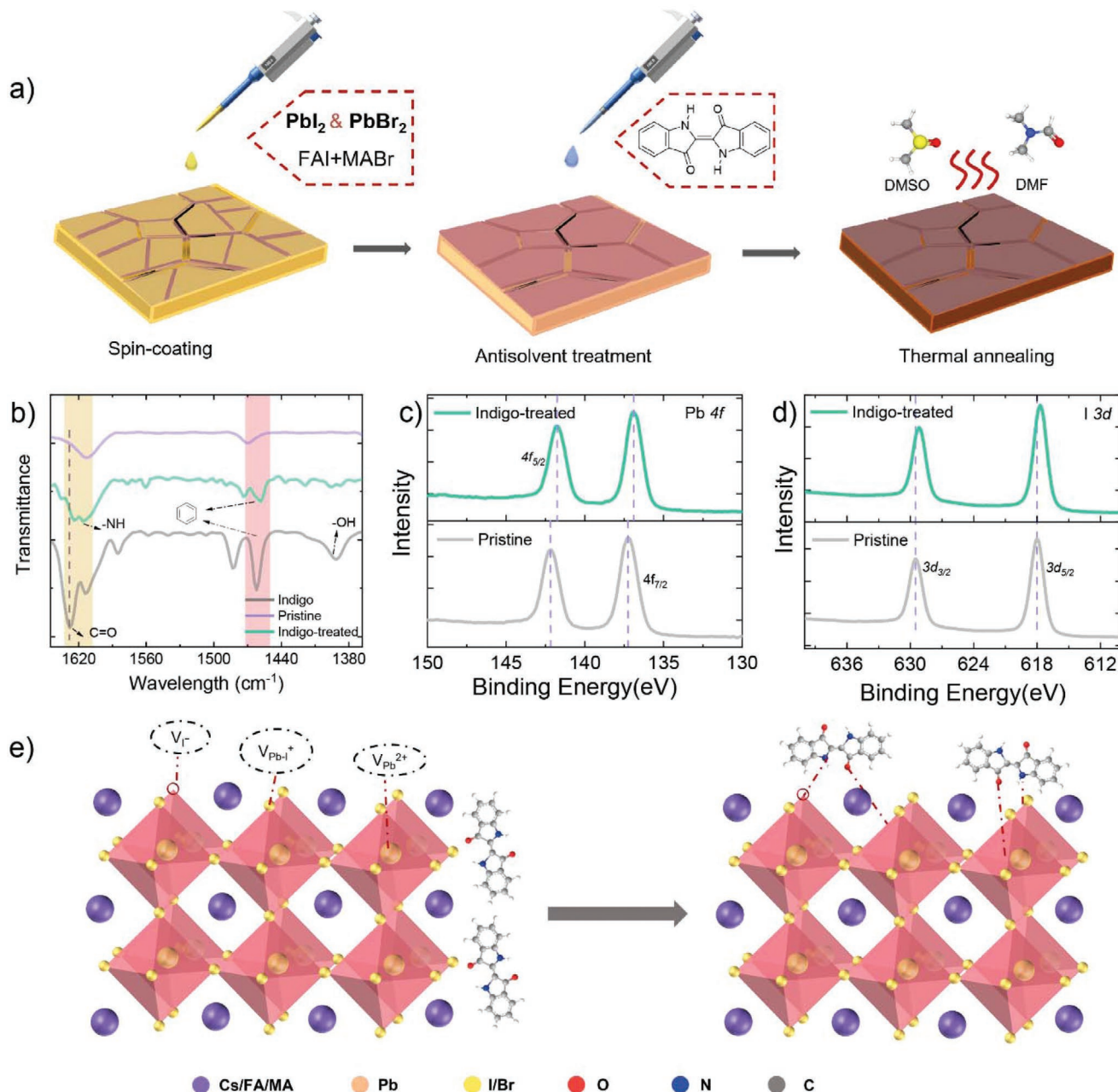


Figure 1. a) Schematic illustration of spin-coating process for fabricating perovskite films with Indigo-assisted antisolvent process, b) FTIR spectra of neat Indigo, pristine, and Indigo passivated perovskites, c) Pb 4f and d) I 3d XPS spectra of pristine and passivated perovskite films, e) schematic illustration of the passivating mechanism between Indigo and mixed hybrid perovskite.

of the molecule on the perovskite surface. Reassuringly, CDD shows that charge is mostly transferred from FAPbI₃ surface Pb ions (e.g., Pb crosslabeled in Figure 2a) to the closest O atoms in the Indigo molecule (i.e., about 0.1 electrons according to the Bader charge analysis). The binding of Indigo molecules on defective FAPbI₃ surfaces containing neutral Pb vacancies is also analyzed (Figure 2b). In this case, the binding energy of the Indigo molecule amounts to -1.58 eV, which indicates a slightly stronger adsorption on the perovskite surface than the nondefective case. When Pb surface vacancies are created, FAPbI₃ surface I⁻ ions start to interact significantly with the

Indigo molecule. For instance, Bader charge analysis indicates that the I ion crosslabeled in Figure 2b, which is closest to the created Pb surface vacancy and O Indigo, donates about ≈ 0.06 electrons to the molecule. In terms of the electronic partial density of states (pDOS, Figure 2c), upon adsorption of the Indigo molecule on the FAPbI₃ surface, the appearance of highly hybridized Indigo O, C, N, I, and Pb electronic orbitals appear close to the Fermi energy level (Figure 2c), which is a clear signature of the formation of perovskite-Indigo molecule chemical bonds. In the case of defective FAPbI₃ surfaces, large hybridizations between FAPbI₃ I and Indigo molecular orbitals appear

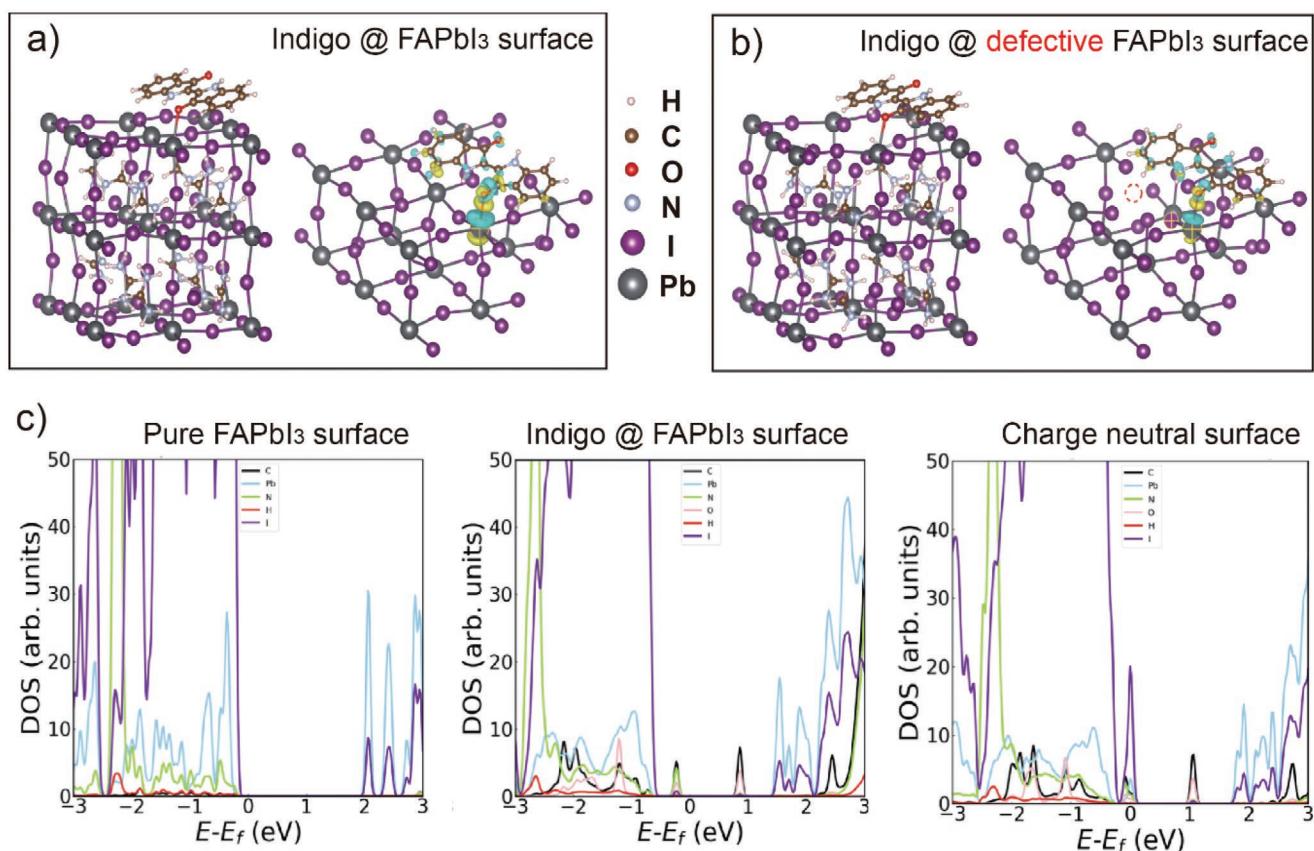


Figure 2. DFT calculated structure and charge density difference (CDD) for Indigo molecule docking on a) stoichiometric FAPbI₃ and b) defective FAPbI₃ surface containing neutral Pb vacancies (indicated with dotted lines in the figure), c) DFT calculated DOS for the relaxed: a) FAPbI₃ surface, b) Indigo@FAPbI₃, c) Indigo@FAPb_{1-x}I₃, the Fermi energy level has been shifted to 0 eV in all the cases.

at the Fermi level (Figure 2c), which is consistent with the strengthening of the perovskite-Indigo molecule interactions driven by the creation of Pb surface vacancies. Overall, our theoretical DFT calculations results confirm that the adsorption of Indigo molecules successfully passivates the FAPbI₃ surface by trapping the unpaired and delocalized electrons stemming from Pb surface ions and vacancies.

In order to further understand the Indigo treatment on the crystallization process and relevant thin film morphology, more measurements on the corresponding perovskite thin films were conducted. Top-view scanning electron microscopy (SEM) images of mixed perovskite films treated with pure CB, CB with Indigo at a concentration of 0.05 and 0.10 mg mL⁻¹ are displayed in Figure 3. The pristine perovskite film shows a smooth morphology with apparent grain boundary, while the Indigo-treated one displays increased crystal domain size and more uniform size distribution than the control sample. The crystal grain further increases at higher Indigo loading concentration, but the uniformity decreased. A similar result was found in the atomic force microscopy (AFM) characterization. As shown in Figure 3d,f, both the surface roughness and the crystal domain size increase after the introduction of Indigo treatment. The larger and more uniform crystal grain size of the mixed perovskite film suggests reduced defects as well as nonradiative recombination centers, which is beneficial for achieving enhanced photovoltaic performance.^[26,45] To

further verify the influence of Indigo on the crystallization of mixed perovskite film, 2D grazing incidence wide-angle X-ray scattering (GIWAXS) was conducted on the corresponding perovskite films.^[31] As shown in Figure 3g,h, after the Indigo treatment, we observe a stronger preference for the diffraction peaks of (110), (112), (202), (220), (222), and (310), especially in the out-of-plane direction. Meanwhile, the X-ray diffraction measurement was also performed on fluorine-doped tin oxide (FTO)/c-TiO₂/Cs_{0.05}FA_{0.85}MA_{0.10}Pb(I_{0.90}Br_{0.10})₃ samples (Figure S3, Supporting Information). All the films show typical patterns of a black perovskite crystal with the characteristic diffraction peak at 13.9° for the (110) phase.^[31,39] Besides, in comparison with the pristine films, the Indigo-modified perovskite films exhibit enhanced diffraction intensity and decreased full width at half maximum, indicating enhanced crystallinity.

To explore the effects of Indigo passivation on the charge dynamics of perovskites, we further performed steady-state photoluminescence (PL) and time-resolved photoluminescence (TRPL) measurements on different perovskite films deposited on the quartz substrates.^[25,35,46] Due to the relatively low Indigo concentration (0.05 mg mL⁻¹), it is not surprising to find that the difference of optical absorption between pristine and indigo treated perovskite films is not significant (Figure S4, Supporting Information). The Indigo-treated perovskite film (0.05 mg mL⁻¹) exhibits largely enhanced PL intensity and a slightly blue-shifted PL peak compared to the control one (Figure 4a). Such

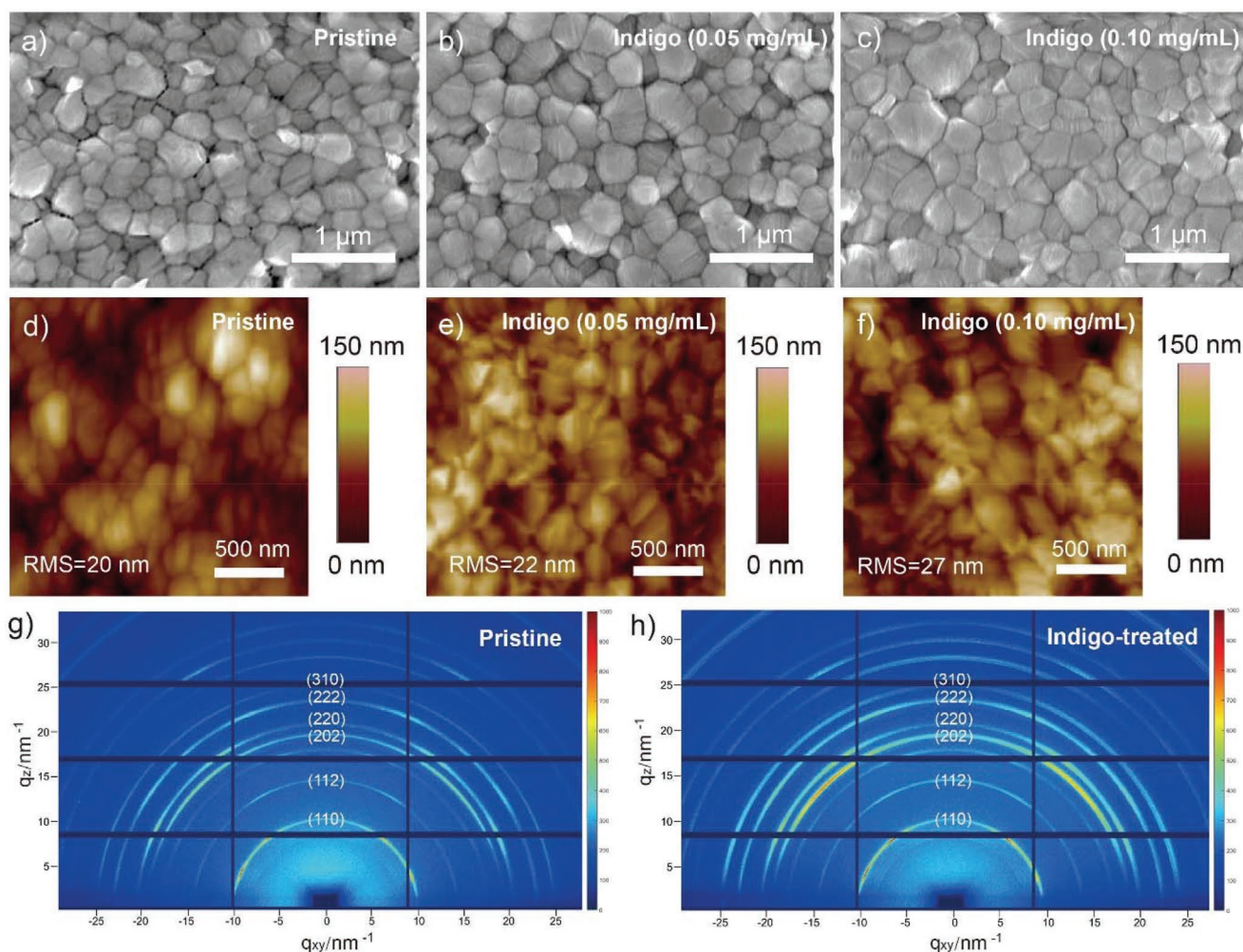


Figure 3. a–c) Top-view SEM images, d–f) AFM images, and g–h) 2D-GIWAXS patterns of pristine and Indigo-treated perovskite films.

a phenomenon is attributed to better passivated perovskite surface and a decrease of spontaneous nonradiative recombination induced by trap states.^[24,47,48] Further increasing the Indigo concentration leads to decreased PL intensity (Figure S5, Supporting Information), which may be attributed to the accumulation of the Indigo molecules.^[49] Meanwhile, we also calculated the lifetime (Table S2, Supporting Information) of charge carriers from the TRPL measurements (Figure 4b). The Indigo treated perovskite film exhibits a longer average lifetime (τ_{ave}) (455 ns for the 0.05 mg mL⁻¹) than the control one (300 ns), suggesting a higher-quality film with suppressed trap-assisted nonradiative recombination.^[50,51] In comparison with the conventional PL spectroscopy, 2D PL mapping imaging allows us to assess the uniformity of the perovskite film (Figure 4c,d). More uniform intensity distribution was found in the Indigo treated perovskite film relative to the pristine one, which may result from the elimination of defects at both the surface and grain boundaries.^[29,47] To investigate the charge transfer dynamics in control and Indigo-treated perovskite films, femtosecond transient absorption (fs-TA) measurements were carried out to collect detailed information for both radiative and nonradiative processes. As shown in Figure 4e,f, the Indigo-treated film

possesses a longer decay time associated with trap states relative to the control one, demonstrating improved charge separation in Indigo-treated films and suggesting that the organic small molecule Indigo can effectively passivate surface trap states and beneficial for reducing nonradiative recombination in perovskite thin film.^[52] All these results confirmed that Indigo passivation can effectively passivate the perovskites, leading to better polycrystalline perovskite films with fewer trap states.

To understand the effect of the Indigo passivation on photovoltaic performance, we fabricated PSCs with a planar n-i-p structure of glass/FTO/TiO₂/Cs_{0.05}FA_{0.85}MA_{0.10}Pb(I_{0.90}Br_{0.10})₃/Spiro-OMeTAD/MoO₃/Ag, as shown in Figure 5a. Each layer of the device can be clearly identified from the cross-sectional SEM image (Figure 5b). The optimization of Indigo concentration is shown in Tables S1 in the Supporting Information. Indigo at a concentration of 0.05 mg mL⁻¹ was found to be the optimal condition, which is in line with the above characterization. Figure 5c shows the current density versus voltage (*J*–*V*) curves of the optimal device with and without the Indigo treatment, under air mass (AM) 1.5G illumination at an intensity of 100 mW cm⁻², with the device parameters summarized in Table 1. The control device shows a best PCE of 20.18% with

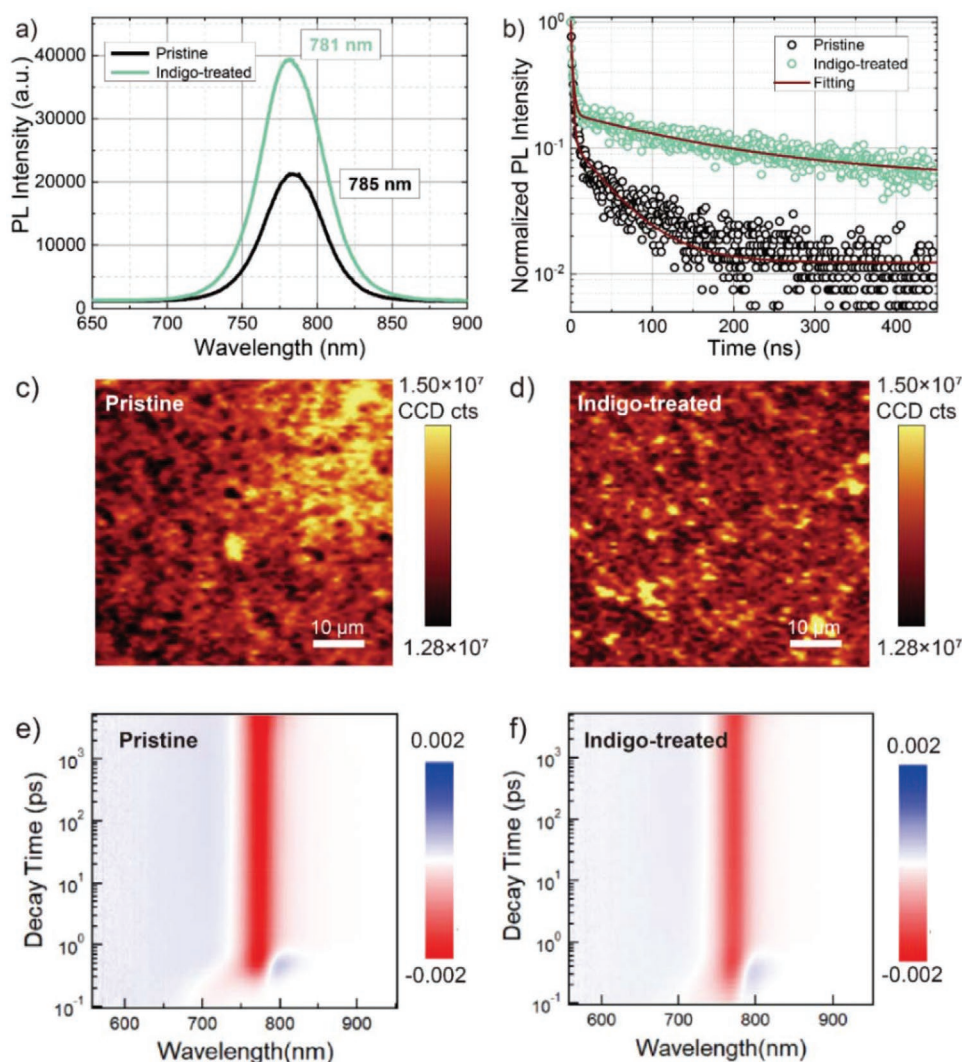


Figure 4. a) Steady-state PL spectra, b) TRPL decay spectra of the perovskite film, c,d) normalized PL mapping of the pristine perovskite film and Indigo-treated perovskite film, and e,f) 2D time-wavelength-dependent TA color maps of pristine and Indigo-treated perovskite films.

a J_{sc} of 24.15 mA cm^{-2} , a V_{oc} of 1.07 V , and a FF of 0.78 , while the champion device after Indigo treatment delivers a significantly improved PCE up to 23.22% with an increased J_{sc} of 25.02 mA cm^{-2} , a V_{oc} of 1.16 , and an FF of 0.80 . Besides, we also achieved large-area PSCs (active area of 1 cm^2) with Indigo (Figure 5d), which outputs an excellent PCE approaching 21% (V_{oc} of 1.14 V , J_{sc} of 24.50 mA cm^{-2} , FF of 0.75 , and PCE of 20.95% , with details shown in Table S3, Supporting Information). In addition, as shown in Figure S6 in the Supporting Information, the control and Indigo-treated cells exhibit steady-state power outputs at the maximum power point of 19.25% and 22.17% , respectively, confirming the reliability of PCE obtained from the $J-V$ measurements. The PCE (Figure 5e) and other device parameters distribution statistics from 24 devices for each case further validates the significant enhancement of device performance and reproducibility. Moreover, the Indigo-treated device exhibits reduced $J-V$ hysteresis effect (hysteresis index = 0.011) relative to the control device (hysteresis index = 0.076). Meanwhile, the incident photon conversion

efficiencies (IPCEs) of the control and Indigo-treated device were also recorded and the results are shown in Figure 5f, the Indigo-treated device exhibits higher values relative to the control device almost across the entire wavelength range ($300\text{--}850 \text{ nm}$), suggesting better charge transport and carrier collection in the device after Indigo passivation. The integrated current density values over the AM 1.5G solar spectrum for control and Indigo-treated cells are 22.98 and 24.05 mA cm^{-2} , respectively, which is in good agreement with the J_{sc} values obtained from the $J-V$ curves.

All these results demonstrate improved charge transport and less charge recombination in the device with Indigo passivation, which is beneficial for improving photovoltaic performance. In addition to photovoltaic efficiency, the stability of perovskite is also a critical issue that affects the further development of PSCs. Here, we evaluated the stability of unencapsulated devices under N_2 environment with continuous $60 \text{ }^\circ\text{C}$ heating and the shelf storage stability under ambient environment ($20 \text{ }^\circ\text{C}$, relative humidity of $35\text{--}45\%$) over 1500 h .^[53] It

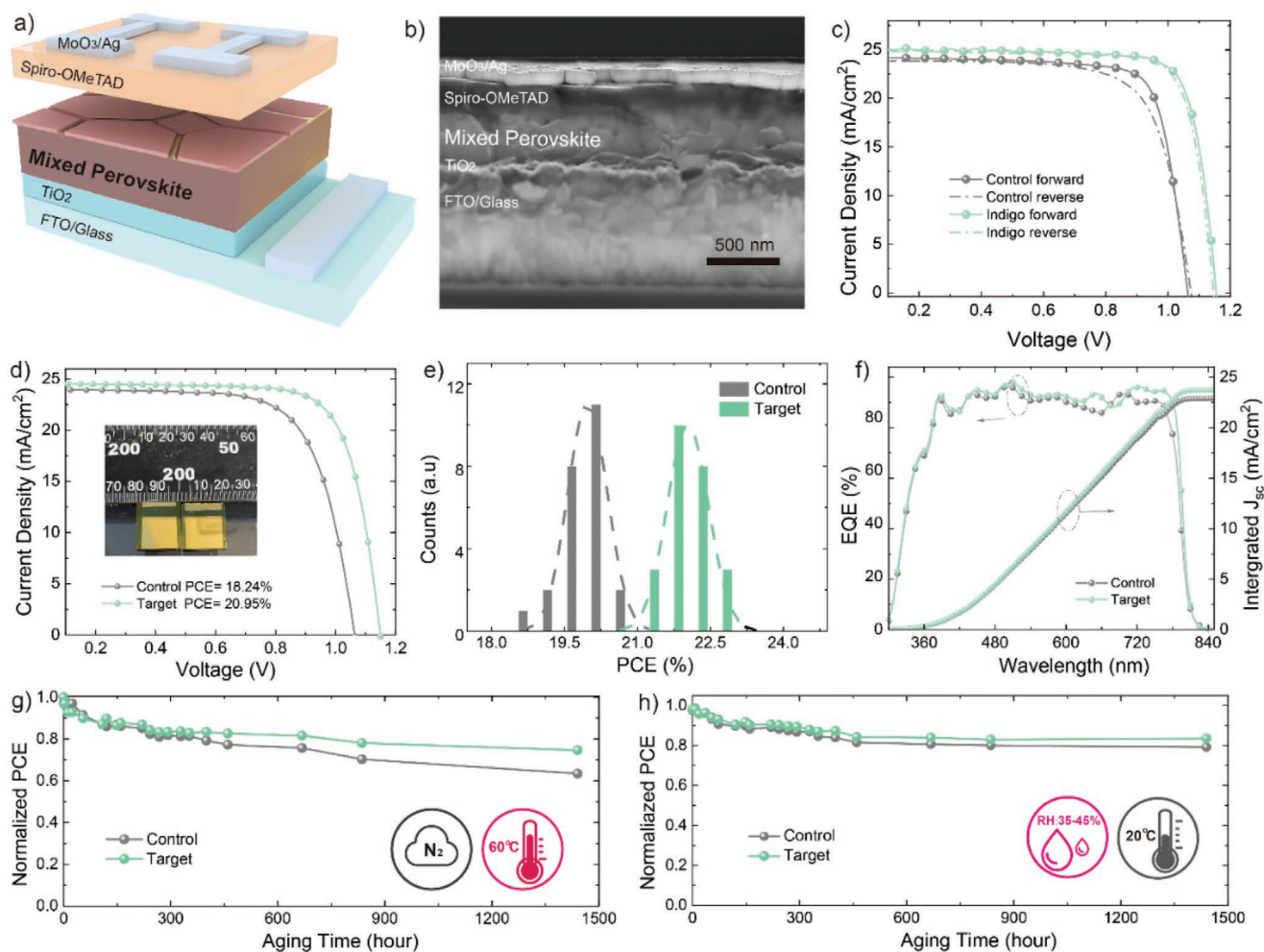


Figure 5. a) Device architecture of PSCs and b) their corresponding cross-sectional SEM image, the scale bar is 500 nm, c) J - V curves of the champion cells, d) the best performance cell with the device area of $1 \times 1 \text{ cm}^2$, e) the PCE histogram of 24 devices, f) J - V curve of the champion cell of Cs_{0.05}FA_{0.85}MA_{0.10}Pb(I_{0.90}Br_{0.10})₃ PSCs, and the inset shows the corresponding EQE spectra, g) long-term stability of unencapsulated Indigo-treated and pristine devices under N₂ environment with continuous 60 °C heating and shelf storage stability exposed in ambient environment (20 °C, relative humidity of 35–45%).

was found that over 75% of the PCE of the Indigo-treated PSCs can be maintained after thermal aging for 1500 h, whereas the control PSCs show a PCE drop of $\approx 40\%$ after the same duration. Moreover, the PCE of the control device drops by $\approx 25\%$ after 1500 h storage under ambient environment without any encapsulation, whereas the devices with Indigo passivation show a PCE drop of only $\approx 15\%$ for the same duration, indicating

that the Indigo post-treatment improves the humidity stability of the PSCs (Figure 5g,h). The contact angle of water drop on control and the Indigo-treated film is presented in Figure S7 in the Supporting Information, indicating enhanced hydrophobic nature after Indigo treatment, which is beneficial for preventing moisture invasion. The rich hydrogen bonds and carbonyl structures in the organic passivating agent can enhance

Table 1. Photovoltaic parameters of the devices based on pristine and Indigo-treated perovskite thin film, the average values were summarized from 24 parallel devices.

Sample		V_{oc} [V]	J_{sc} [mA cm ⁻²]	FF	PCE [%]
Control	Forward	1.07	24.15	0.78	20.18
	Reserve	1.07	23.87	0.73	18.64
	Average	1.06 ± 0.03	23.92 ± 0.26	0.76 ± 0.01	19.45 ± 0.46
Indigo	Forward	1.16	25.02	0.80	23.22
	Reserve	1.15	24.74	0.80	22.97
	Average	1.15 ± 0.01	24.85 ± 0.36	0.79 ± 0.01	22.80 ± 0.42

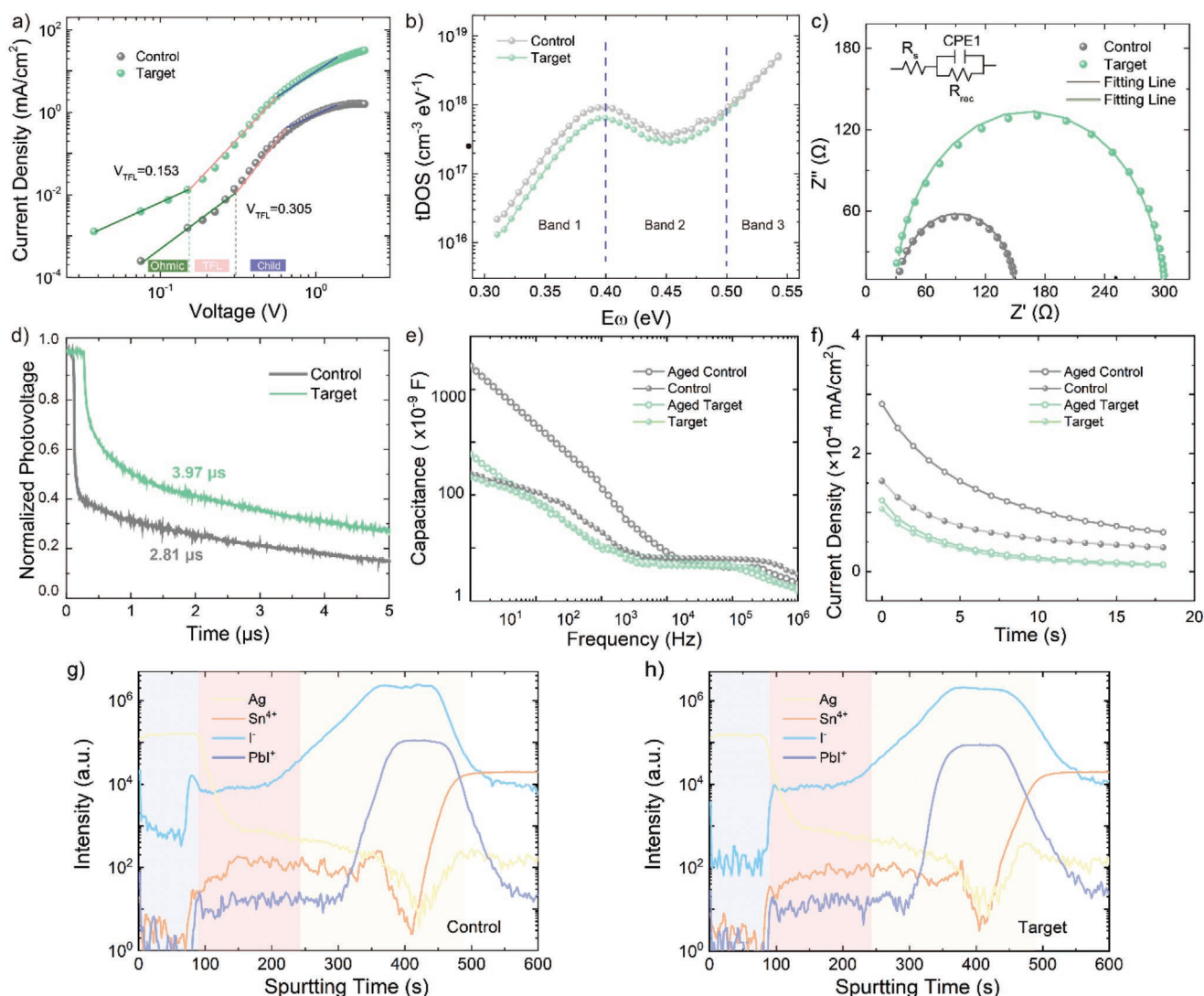


Figure 6. a) SCLC measurements of hole-only devices, b) the trap density of states (t-DOS) of control and target device calculated from the frequency-dependent capacitance plot, c) Nyquist plots of the optimized target and control devices, d) transient photovoltage (TPV) decay spectra of the Indigo-treated and control devices, e) the C–F profiles of the fresh and aged PSCs, f) transient ion current for extracting mobile ion concentration of the fresh and aged PSCs, effect of Indigo for suppressing the migration of ionic in perovskite film, TOF-SIMS elemental depth profiles of Ag, Sn⁴⁺, I⁻, and PbI⁺ of the g) control and h) target device.

device stability both in terms of humidity and thermal stress, which have been reported in recent works.^[19,38] Herein, we present a simple yet efficient pathway using abundant and low-cost natural organic dyes to achieve high-performance perovskite solar cells.

Finally, we characterized the control and Indigo-treated solar cells to understand the kinetics behind enhanced device performance. The space-charge-limited current (SCLC) characterization was employed to study the defect density of perovskite films after the Indigo passivation. The *J*–*V* curves of the hole-only device with a structure of glass/FTO/poly(3,4-ethylenedioxythiophene):poly(styrenesulfonate)/perovskite/Spiro-OMeTAD/MoO₃/Ag are shown in **Figure 6a**. The linear relation indicates an ohmic response of the device in the region of low bias voltage, while the current increases quickly as the voltage goes up and exceeds the kink point, where the trap-states are fully

filled.^[25] And the trap-state density (n_t) can be calculated from the trap-filled limit voltage (V_{TFL}) using the equation

$$n_t = \frac{2\epsilon\epsilon_0 V_{TFL}}{eL^2} \quad (2)$$

where ϵ is the relative dielectric constant of perovskite, ϵ_0 is the vacuum permittivity, and L is the thickness of the perovskite layer. The V_{TFL} of control and target device is 0.305 and 0.153 V, giving a corresponding n_t values of $1.20 \times 10^{17} \text{ cm}^{-3}$ and $6.02 \times 10^{16} \text{ cm}^{-3}$, respectively. The lower value for the target device indicates that the hole trap state density of perovskite thin films is greatly reduced after the Indigo passivation.^[39] Moreover, the trap density of state (tDOS) in the device was also characterized by thermal admittance spectroscopy measurements (Figure 6b). It is obvious that the trap density of target device is lower than that of control one at the shallow trap

region. Meanwhile, The J_{sc} and V_{oc} as a function of illumination intensity were measured. Figure S8 in the Supporting Information shows the values of the exponential factor (α) is 0.98 and 0.99 for the control and target devices, respectively, indicating both devices exhibit similar bimolecular recombination. For a better comparison, the light intensity dependence on V_{oc} was also studied. If the slope is greater than $1 kT/q$ (where k is the Boltzmann constant, T is the temperature, and q is the elementary charge), the interfacial trap-assisted Shockley–Read–Hall (SRH) recombination should be dominant.^[54] The slope of target device is $1.57 kT/q$, which is lower than that of the control device ($1.86 kT/q$), indicating that the trap-assisted SRH recombination process at the charge collection interfaces has been effectively suppressed though the Indigo passivation (Figure S9, Supporting Information). Furthermore, to fully understand the improvement of the V_{oc} , electrochemical impedance spectroscopy was utilized to study the charge-transfer resistance (R_{tr}) and recombination resistance (R_{rec}) in these devices. The Nyquist plots of the control target devices are shown in Figure 6c, with the parameters listed in Table S4 in the Supporting Information. The Indigo treated target device shows a reduced R_{tr} (30.39 Ω) and an increased R_{rec} (267.2 Ω), indicating that Indigo passivation can suppress the carrier recombination and improve the charge transfer at the interface, which is consistent with the increased V_{oc} and J_{sc} . Similar conclusion can be found from the dark J – V characteristics (Figure S10, Supporting Information), where the leakage current for the target device is decreased compared to that of the control one, suggesting suppressed interfacial recombination. In addition, Mott–Schottky analysis of the capacitance–voltage (C – V) curves was employed to investigate the built-in potential (V_{bi}) and the width of depletion region of control and target solar cells (Figure S11, Supporting Information). The Indigo-treated device exhibits higher V_{bi} 0.958 V than the 0.924 V of pristine device, which indicates a wider depletion layer to accelerate charge carrier separation and promote charge transport.^[37,47] Meanwhile, transient photovoltage (TPV) measurements were performed on both devices (Figure 6d). The target device shows a photovoltage decay time of 3.97 μ s, which is longer than 2.81 μ s for the control device, suggesting that the Indigo passivation can suppress nonradiation recombination and deliver a faster charge transport rate. All these results indicate that the intrinsic mechanism of enhancement of photovoltaic performance lies in the improvement of the interfaces, which can be attributed to the Indigo molecular passivation. To gain more insight to the effect of Indigo passivation on ions migration in PSC, a set of characterizations including capacitance–frequency (C – F), transient ionic current and time-of-flight secondary ion mass spectrometry (TOF-SIMS) were performed. Figure 6e indicates that the fresh devices (control and Indigo-treated) have a similar capacitance throughout a wide frequency range. In contrast, the control device shows an apparent increase in capacitance at low frequency relative to the Indigo-treated one aged in ambient environment (20–30 $^{\circ}$ C, 25% relative humidity) for 5 d, indicating the accumulation of mobile ions in aged control device. Furthermore, the transient ionic current was conducted to calculate the mobile ion concentrations in perovskite under dark condition after applying an external forward bias at V_{oc} for 10 s. It is known that the current was mainly contributed by the redistribution

of mobile ions in the perovskite under dark condition.^[55] As shown in Figure 6f, the device of Indigo-treated has much lower current and shorter decay time as compared to the control device. We could estimate the concentration of mobile ionic from transient ionic current in perovskite by using the formula

$$n = \frac{\int_{t_1}^{t_2} Idt}{eL} \quad (3)$$

where n is the ion concentration, t is the time, I is the current density, e is the elementary charge, and L is the thickness of perovskite film. The calculated ion concentration for Indigo-treated device and control one is 8.8×10^{16} and 1.01×10^{17} cm^{-3} , respectively, which is much lower than the corresponding aged one (1.92×10^{17} and 3.63×10^{17} cm^{-3}), suggesting that the Indigo-treatment can suppress the ion migration and degradation of perovskite film. Meanwhile, to detect the vertical thin-film information in PSCs w/o Indigo treatment, TOF-SIMS was performed on devices with a structure of FTO/SnO₂/Perovskite/Spiro-OMeTAD/MoO₃/Ag. The TiO₂ was replaced by SnO₂ because the Sn⁴⁺ element has higher sensitivity and easier to be detected, and such a modification has a negligible influence on the ion migration investigations. In addition, As shown in Figure 6g,h, we chose to monitor Ag, Sn⁴⁺, I[−], and PbI⁺, which could determine the interface of each layer and study the I[−] ion migration. For the control device, as shown in Figure 6g, it is obvious that the I[−] ions remarkably diffuses into the Spiro-OMeTAD and Ag electrode from the perovskite layer, in contrast, the Indigo-treated device shows negligible I[−] ions diffusion into Ag electrode (Figure 6h). In addition, through comparing the distribution of I[−] and PbI⁺ with in the perovskite active layer, we find the diffusion trend of I[−] toward hole transport layer in the control device, further confirming retarded ion migration through Indigo passivation. These observations indicate the interaction between Indigo and halide perovskite could suppress the formation of defects, which is considered as the dominate channels for ions migration.^[56] The combined TOF-SIMS, capacitance and ionic current measurement results confirm that the ion dissociation and migration were effectively suppressed by the natural molecular passivator Indigo.

3. Conclusion

In conclusion, we have demonstrated a new strategy of Indigo molecular passivation for the design and preparation of high-quality hybrid perovskite films for photovoltaic applications. Through dissolving functional Indigo molecules in chlorobenzene at the optimal concentrations to treat the Cs_{0.05}FA_{0.85}MA_{0.10}Pb(I_{0.90}Br_{0.10})₃ perovskite films, we proved that the existence of both C=O/–NH functional groups is important for the passivation of defects in the pristine perovskite films. Combined theoretical and experimental results confirmed that the strong interactions between Indigo molecules and perovskite surfaces via Lewis base/acid coordination effectively reduces the thin film defects and suppress trap-assisted nonradiative recombination. Moreover, with the assistance of Indigo passivation, the resultant perovskite film displays better morphology with increased crystal domain size and more

uniform size distribution than the pristine one. These superior qualities enable an excellent PCE of 23.22% for Indigo-treated PSCs with retarded ion migration, in comparison to that of 20.18% in the control device. Besides, a champion PCE of 20.95% was obtained for large-area device (1 cm²) after Indigo passivation. Furthermore, the carbonyl groups and hydrogen bonds structures in the Indigo dye can significantly enhance device stability both in terms of humidity and thermal stress. More importantly, the abundant availability of Indigo in nature will make it a desired low-cost material for application in stable and efficient solar cells based on hybrid halide perovskite.

4. Experimental Section

Preparation and Characterization of Perovskite Solar Cells: First, the FTO glass substrates were sequentially cleaned with detergent water, acetone and isopropanol for 1 h and then dried with N₂. Then the clean FTO as the substrate were used for deposition of titanium dioxide. After treated under ultraviolet light and ozone for about 15 min, the FTO glasses were immersing in 200 mL ultrapure water with 4.5 mL titanium tetrachloride for 60 min at 70 °C. Further, the FTO substrates coated with TiO₂ was washed by distilled water and then annealed at 180 °C for 30 min. After treated by ultraviolet ozone for 15 min, the structures were transferred into nitrogen glove box (O₂ and H₂O both below 2.0 ppm). For the deposition of perovskite thin films, a 30 μL of 1.20 M Cs_{0.05}FA_{0.85}MA_{0.10}Pb(I_{0.90}Br_{0.10})₃ precursor solution was spin-coating onto the c-TiO₂ layer at the speed 1000 rpm for 10 s (acceleration rate at 200 rpm s⁻¹) and 4000 rpm for 20 s (acceleration rate at 2000 rpm s⁻¹). During the second stage of spin-coating (high speed) process, the antisolvent which contains different concentrations of Indigo was dripped (at 8 s) onto the perovskite surface. Before depositing the perovskite layer, the glove box was purged in N₂ for minimizing solvent residues of CB. Next, the as-deposited perovskite films were annealed at 100 °C for 60 min and the color of the films were converted from gold to black in this process. After cooling down the films to room temperature, the hole transport solution Spiro-OMeTAD (contains 90 mg Spiro-OMeTAD, 35.5 μL of a 520 mg mL⁻¹ lithium bis(trifluoro-methylsulfonyl) imide in acetonitrile and 20.6 μL of 4-tert-butylpyridine in 1 mL of chlorobenzene) was spin-coated onto the perovskite/c-TiO₂/FTO substrate at 4000 rpm for 20 s to produce about 200 nm of hole transport layer. Finally, 8 nm MoO₃ and 120 nm Ag was deposited by thermal vacuum evaporation under 10⁻⁶ mbar. Also, the current density–voltage (*J*–*V*) characteristics of the solar cells was measured using a Keithley 2400 Digital Source Meter and simulated AM 1.5G spectrum at 100 mW cm⁻² with a solar simulator (Class AAA, 94023A-U, Newport) in the ambient atmosphere. Before test, the light intensity of the Xenon lamp was calibrated with a standard silicon solar cell (91150 V, Newport Oriol). The active area of 7.25 mm² was defined by a shadow mask. The external quantum efficiency (EQE) measurement of the solar cells was characterized on a Solar Cell Scan 100 system (Zolix Instruments Co. Ltd.).

Supporting Information

Supporting Information is available from the Wiley Online Library or from the author.

Acknowledgements

This work was supported by the National Key Research and Development Program of China (2019YFE0108600), National Natural Science Foundation of China (52073198, 22161142003, and 61911530158), Natural Science Foundation of Jiangsu Province (BK20211598), Science

and Technology Program of Jiangsu Province (BZ2020011), Science and Technology Program of Suzhou (SYG202037), “111” project, the China Postdoctoral Science Foundation (Grant No. 2021T140495), Collaborative Innovation Center of Suzhou Nano Science and Technology, Soochow University. C.C. acknowledges support from the Spanish Ministry of Science, Innovation, and Universities under the “Ramon y Cajal” fellowship RYC2018-024947-I.

Conflict of Interest

The authors declare no conflict of interest.

Data Availability Statement

The data that support the findings of this study are available from the corresponding author upon reasonable request.

Keywords

indigo, long-term stability, natural dyes, passivation, perovskite solar cells

Received: February 15, 2022

Revised: March 20, 2022

Published online:

- [1] N. J. Jeon, J. H. Noh, Y. C. Kim, W. S. Yang, S. Ryu, S. I. Seok, *Nat. Mater.* **2014**, *13*, 897.
- [2] H. Zhou, Q. Chen, G. Li, S. Luo, T. B. Song, H. S. Duan, Z. Hong, J. You, Y. Liu, Y. Yang, *Science* **2014**, *345*, 542.
- [3] G. Kim, H. Min, K. S. Lee, D. Y. Lee, S. M. Yoon, S. I. Seok, *Science* **2020**, *370*, 108.
- [4] H. Lu, Y. Liu, P. Ahlawat, A. Mishra, W. R. Tress, F. T. Eickemeyer, Y. Yang, F. Fu, Z. Wang, C. E. Avalos, B. I. Carlsen, A. Agarwalla, X. Zhang, X. Li, Y. Zhan, S. M. Zakeeruddin, L. Emsley, U. Rothlisberger, L. Zheng, A. Hagfeldt, M. Gratzel, *Science* **2020**, *370*, 8985.
- [5] H. Min, M. Kim, S. U. Lee, H. Kim, G. Kim, K. Choi, J. H. Lee, S. I. Seok, *Science* **2019**, *366*, 749.
- [6] A. Younis, C. H. Lin, X. Guan, S. Shahrokhi, C. Y. Huang, Y. Wang, T. He, S. Singh, L. Hu, J. R. D. Retamal, J. H. He, T. Wu, *Adv. Mater.* **2021**, *33*, 2005000.
- [7] J. J. Yoo, G. Seo, M. R. Chua, T. G. Park, Y. Lu, F. Rotermund, Y. K. Kim, C. S. Moon, N. J. Jeon, J. P. Correa-Baena, V. Bulovic, S. S. Shin, M. G. Bawendi, J. Seo, *Nature* **2021**, *590*, 587.
- [8] M. Jeong, I. W. Choi, E. M. Go, Y. Cho, M. Kim, B. Lee, S. Jeong, Y. Jo, H. W. Choi, J. Lee, J. H. Bae, S. K. Kwak, D. S. Kim, C. Yang, *Science* **2020**, *369*, 1615.
- [9] H. Min, D. Y. Lee, J. Kim, G. Kim, K. S. Lee, J. Kim, M. J. Paik, Y. K. Kim, K. S. Kim, M. G. Kim, T. J. Shin, S. I. Seok, *Nature* **2021**, *598*, 444.
- [10] J. G. Sun, F. C. Li, J. Y. Yuan, W. L. Ma, *Small Methods* **2021**, *5*, 2100046.
- [11] M. Kim, G. H. Kim, T. K. Lee, I. W. Choi, H. W. Choi, Y. Jo, Y. J. Yoon, J. W. Kim, J. Lee, D. Huh, H. Lee, S. K. Kwak, J. Y. Kim, D. S. Kim, *Joule* **2019**, *3*, 2179.
- [12] Y. An, J. Hidalgo, C. A. R. Perini, A. F. Castro-Mendez, J. N. Vagott, K. Bairley, S. R. Wang, X. G. Li, J. P. Correa-Baena, *ACS Energy Lett.* **2021**, *6*, 1942.

- [13] J. B. Li, R. Munir, Y. Y. Fan, T. Q. Niu, Y. C. Liu, Y. F. Zhong, Z. Yang, Y. S. Tian, B. Liu, J. Sun, D. M. Smilgies, S. Thoroddsen, A. Amassian, K. Zhao, S. Z. Liu, *Joule* **2018**, *2*, 1313.
- [14] P. Y. Liu, H. M. Xiang, W. Wang, R. Ran, W. Zhou, Z. P. Shao, *J. Energy Chem.* **2021**, *62*, 243.
- [15] S. W. Kim, G. Kim, C. S. Moon, T. Y. Yang, J. Seo, *Small Methods* **2021**, *5*, 2001248.
- [16] Q. Yang, X. Liu, S. Yu, Z. Feng, L. Liang, W. Qin, Y. Wang, X. Hu, S. Chen, Z. Feng, G. Hou, K. Wu, X. Guo, C. Li, *Energy Environ. Sci.* **2021**, *14*, 6536.
- [17] Y. Zhang, Y. Wang, L. Zhao, X. Yang, C.-H. Hou, J. Wu, R. Su, S. Jia, J.-J. Shyue, D. Luo, P. Chen, M. Yu, Q. Li, L. Li, Q. Gong, R. Zhu, *Energy Environ. Sci.* **2021**, *14*, 6526.
- [18] R. Wang, J. Xue, K. L. Wang, Z. K. Wang, Y. Luo, D. Fenning, G. Xu, S. Nuryyeva, T. Huang, Y. Zhao, J. L. Yang, J. Zhu, M. Wang, S. Tan, I. Yavuz, K. N. Houk, Y. Yang, *Science* **2019**, *366*, 1509.
- [19] X. P. Zheng, B. Chen, J. Dai, Y. J. Fang, Y. Bai, Y. Z. Lin, H. T. Wei, X. C. Zeng, J. S. Huang, *Nat. Energy* **2017**, *2*, 17102.
- [20] S. Yang, S. Chen, E. Mosconi, Y. Fang, X. Xiao, C. Wang, Y. Zhou, Z. Yu, J. Zhao, Y. Gao, F. De Angelis, J. Huang, *Science* **2019**, *365*, 473.
- [21] X. Y. Yang, Y. Ni, Y. Z. Zhang, Y. J. Wang, W. Q. Yang, D. Y. Luo, Y. G. Tu, Q. H. Gong, H. F. Yu, R. Zhu, *ACS Energy Lett.* **2021**, *6*, 2404.
- [22] M. J. Jeong, K. M. Yeom, S. J. Kim, E. H. Jung, J. H. Noh, *Energy Environ. Sci.* **2021**, *14*, 2419.
- [23] Y. Cai, J. Cui, M. Chen, M. Zhang, Y. Han, F. Qian, H. Zhao, S. Yang, Z. Yang, H. Bian, T. Wang, K. Guo, M. Cai, S. Dai, Z. Liu, S. Liu, *Adv. Funct. Mater.* **2020**, *31*, 2005776.
- [24] L. Wen, Y. Rao, M. Zhu, R. Li, J. Zhan, L. Zhang, L. Wang, M. Li, S. Pang, Z. Zhou, *Angew. Chem., Int. Ed.* **2021**, *60*, 17356.
- [25] Q. He, M. Worku, H. Liu, E. Lochner, A. J. Robb, S. Lteif, J. S. R. Vellore Winfred, K. Hanson, J. B. Schlenoff, B. J. Kim, B. Ma, *Angew. Chem., Int. Ed.* **2021**, *60*, 2485.
- [26] Y. Li, J. Shi, J. Zheng, J. Bing, J. Yuan, Y. Cho, S. Tang, M. Zhang, Y. Yao, C. F. J. Lau, D. S. Lee, C. Liao, M. A. Green, S. Huang, W. Ma, A. W. Y. Ho-Baillie, *Adv. Sci.* **2020**, *7*, 1903368.
- [27] S. Chen, X. Xiao, B. Chen, L. L. Kelly, J. Zhao, Y. Lin, M. F. Toney, J. Huang, *Sci. Adv.* **2021**, *7*, 2412.
- [28] Y. H. Chen, S. Q. Tan, N. X. Li, B. L. Huang, X. X. Niu, L. Li, M. Z. Sun, Y. Zhang, X. Zhang, C. Zhu, N. Yang, H. C. Zai, Y. L. Wu, S. Ma, Y. Bai, Q. Chen, F. Xiao, K. W. Sun, H. P. Zhou, *Joule* **2020**, *4*, 1961.
- [29] X. Zhu, M. Du, J. Feng, H. Wang, Z. Xu, L. Wang, S. Zuo, C. Wang, Z. Wang, C. Zhang, X. Ren, S. Priya, D. Yang, S. F. Liu, *Angew. Chem., Int. Ed.* **2021**, *60*, 4238.
- [30] J. Zhu, S. Park, O. Y. Gong, C. Sohn, Z. Li, Z. Zhang, B. Jo, W. Kim, G. S. Han, D. H. Kim, T. K. Ahn, J. Lee, H. S. Jung, *Energy Environ. Sci.* **2021**, *14*, 4903.
- [31] J. G. Sun, X. L. Zhang, X. F. Ling, Y. G. Yang, Y. Wang, J. J. Guo, S. Z. Liu, J. Y. Yuan, W. L. Ma, *J. Mater. Chem. A* **2021**, *9*, 23019.
- [32] X. Zhao, T. Liu, A. B. Kaplan, C. Yao, Y. L. Loo, *Nano Lett.* **2020**, *20*, 8880.
- [33] Q. Hu, W. Chen, W. Q. Yang, Y. Li, Y. C. Zhou, B. W. Larson, J. C. Johnson, Y. H. Lu, W. K. Zhong, J. Q. Xu, L. Klivansky, C. Wang, M. Salmeron, A. B. Djuricic, F. Liu, Z. B. He, R. Zhu, T. P. Russell, *Joule* **2020**, *4*, 1575.
- [34] A. D. Taylor, Q. Sun, K. P. Goetz, Q. An, T. Schramm, Y. Hofstetter, M. Litterst, F. Paulus, Y. Vaynzof, *Nat. Commun.* **2021**, *12*, 1878.
- [35] F. Li, J. Yuan, X. Ling, Y. Zhang, Y. Yang, S. H. Cheung, C. H. Y. Ho, X. Gao, W. Ma, *Adv. Funct. Mater.* **2018**, *28*, 1870119.
- [36] F. Cheng, R. He, S. Nie, C. Zhang, J. Yin, J. Li, N. Zheng, B. Wu, *J. Am. Chem. Soc.* **2021**, *143*, 5855.
- [37] R. Chen, Y. Wang, S. Nie, H. Shen, Y. Hui, J. Peng, B. Wu, J. Yin, J. Li, N. Zheng, *J. Am. Chem. Soc.* **2021**, *143*, 10624.
- [38] Z. Zhang, Y. Gao, Z. Li, L. Qiao, Q. Xiong, L. Deng, Z. Zhang, R. Long, Q. Zhou, Y. Du, Z. Lan, Y. Zhao, C. Li, K. Mullen, P. Gao, *Adv. Mater.* **2021**, *33*, 2008405.
- [39] L. Yang, Q. Xiong, Y. Li, P. Gao, B. Xu, H. Lin, X. Li, T. Miyasaka, *J. Mater. Chem. A* **2021**, *9*, 1574.
- [40] S. Li, Z. Yuan, J. Y. , P. Deng, Q. Zhang, B. Sun, *J. Mater. Chem. A* **2014**, *2*, 5427.
- [41] S. Wang, Z. Zhang, Z. Tang, C. Su, W. Huang, Y. Li, G. Xing, *Nano Energy* **2021**, *82*, 105712.
- [42] C. Cazorla, J. Boronat, *Rev. Mod. Phys.* **2017**, *89*, 035003.
- [43] J. P. Perdew, K. Burke, M. Ernzerhof, *Phys. Rev. Lett.* **1996**, *77*, 3865.
- [44] P. E. Blochl, *Phys. Rev. B: Condens. Matter* **1994**, *50*, 17953.
- [45] Y. P. Xiao, W. W. Zheng, B. Yuan, C. Wen, M. Lanza, *Cryst. Res. Technol.* **2021**, *56*, 2100056.
- [46] Y. W. Jang, S. Lee, K. M. Yeom, K. Jeong, K. Choi, M. Choi, J. H. Noh, *Nat. Energy* **2021**, *6*, 63.
- [47] Q. Zhou, Y. Gao, C. Cai, Z. Zhang, J. Xu, Z. Yuan, P. Gao, *Angew. Chem., Int. Ed.* **2021**, *60*, 8303.
- [48] X. Ling, J. Yuan, X. Zhang, Y. Qian, S. M. Zakeeruddin, B. W. Larson, Q. Zhao, J. Shi, J. Yang, K. Ji, Y. Zhang, Y. Wang, C. Zhang, S. Duhm, J. M. Luther, M. Gratzel, W. Ma, *Adv. Mater.* **2020**, *32*, 2001906.
- [49] M. Yang, T. Tian, W. Feng, L. Wang, W.-Q. Wu, *Acc. Mater. Res.* **2021**, *2*, 1141.
- [50] X. Ling, H. Zhu, W. Xu, C. Liu, L. Pan, D. Ren, J. Yuan, B. W. Larson, C. Gratzel, A. R. Kirmani, O. Ouellette, A. Krishna, J. Sun, C. Zhang, Y. Li, S. M. Zakeeruddin, J. Gao, Y. Liu, J. R. Durrant, J. M. Luther, W. Ma, M. Gratzel, *Angew. Chem., Int. Ed.* **2021**, *60*, 27299.
- [51] Y. Zhang, Y. Li, L. Zhang, H. Hu, Z. Tang, B. Xu, N. G. Park, *Adv. Energy Mater.* **2021**, *11*, 2102538.
- [52] L. Hu, Q. Zhao, S. Huang, J. Zheng, X. Guan, R. Patterson, J. Kim, L. Shi, C. H. Lin, Q. Lei, D. Chu, W. Tao, S. Cheong, R. D. Tilley, A. W. Y. Ho-Baillie, J. M. Luther, J. Yuan, T. Wu, *Nat. Commun.* **2021**, *12*, 466.
- [53] E. Ochoa-Martinez, J. V. Milic, *Nat. Energy* **2021**, *6*, 858.
- [54] C. Zhang, H. Wang, H. Li, Q. Zhuang, C. Gong, X. Hu, W. Cai, S. Zhao, J. Chen, Z. Zang, *J. Energy Chem.* **2021**, *63*, 452.
- [55] Y. Ma, Y. Cheng, X. Xu, M. Li, C. Zhang, S. H. Cheung, Z. Zeng, D. Shen, Y. Xie, K. L. Chiu, F. Lin, S. K. So, C. Lee, S. Tsang, *Adv. Funct. Mater.* **2021**, *31*, 2006802.
- [56] D. Wei, F. Ma, R. Wang, S. Dou, P. Cui, H. Huang, J. Ji, E. Jia, X. Jia, S. Sajid, A. M. Elseman, L. Chu, Y. Li, B. Jiang, J. Qiao, Y. Yuan, M. Li, *Adv. Mater.* **2018**, *30*, 1707583.